Active Power Decoupling Method for DC to Single-phase AC Converter Utilizing Triangular Current Mode

Hiroki Watanabe
Dept. of Electrical, Electronics and Information Engineering
Nagaoka University of Technology
Nagaoka, Niigata, Japan
hwatanabe@vos.nagaokaut.ac.jp

Jun-ichi Itoh
Dept. of Electrical, Electronics and Information Engineering
Nagaoka University of Technology
Nagaoka, Niigata, Japan
itoh@vos.nagaokaut.ac.jp

***Abstract*—This paper proposes an active power decoupling control with the Zero Voltage Switching (ZVS) using the Triangular Current Mode (TCM) for photovoltaic micro-inverter applications. In single-phase AC converter applications, it is known that the double-line frequency power ripple increases the volume of the DC-link capacitor. On the other hand, TCM is the most simple and effective method to achieve ZVS for many converters. However, the open-loop based TCM has the drawback for the accuracy of the average current control since the current error is caused by the parameter mismatch including the switching timing error. This paper proposes the closed-loop based TCM control in order to achieve the both of the active power decoupling control and the improved average current control. The proposed TCM control compensates the current error between the current command and the actual current with the feedback loop. Furthermore, the second-order harmonics due to the power ripple is also compensated by the proposed control. According to simulation results, it was confirmed that the current error of 32.3% was compensated by the proposed control. Finally, the second-order harmonics was reduced by 96.0%.**

Keywords—Photovoltaic (PV) micro-inverter, Active power decoupling, Triangular current mode

I. INTRODUCTION

Recently, PV market has been greatly grown for realization of sustainable energy solutions. In the PV systems, grid-tied-PV inverters are typically accepted for the grid-connected operation and the maximum-power-point tracking operation. The configuration of the grid-tied-PV inverter is classified as a centralized inverter and a micro-inverter. The centralized-inverter has the power capacity of several kilo-watts, and it receives the generated power from a number of PV modules. On the other hand, the power capacity of the micro-inverters is several hundred-watts because the micro-inverters are placed behind the PV modules. The micro-inverters have attractive advantages compared to the centralized inverter, e.g., 1) improvement of system efficiency, 2) easy installation, 3) low manufacturing cost. Especially, micro-inverters optimize the generated power on each PV modules by the Maximum Power Point Tracking (MPPT) in order to avoid the decrease of the generated power due to shadows. According to these reason, the micro-inverters has the possibility of becoming future major-PV-systems [1]-[6].

The micro-inverters are used as the interface converter between the PV modules and the single-phase grid. In this case, the high voltage gain is require because the PV input voltage becomes low compared to the centralized inverter. In addition, the micro-inverters require the galvanic isolation for the electrical safety for users. Therefore, the isolated converter topologies such as the flyback converter are commonly accepted for micro-inverters [7]. Especially, the active clamp circuit and quasi-resonant operation contribute the reduction of snubber losses and switching losses. On the other hand, a DC-DC transformer (DCX) has been considered for some applications [8]-[9]. DCX reduces the volume of the transformer owing to the high switching frequency operation. In particular, the Zero Voltage Switching (ZVS) and Zero Current Switching (ZCS) are adopted in order to reduce the switching losses. Because of these reasons, a LLC converter, Dual Active Bridge (DAB) converter, Series Resonant (SR) converter are widely considered for DCX.

The single-phase converter application has the drawback that is instantaneous power ripple. The double-line frequency power ripple occurs by the twice of the grid frequency, and it becomes reason of MPPT failure. Therefore, the energy buffer is placed in the power converter in order to decouple the input and output power. Usually, a bulky electrolytic capacitor is used as the energy buffer for the power decoupling. However, the electrolytic capacitor becomes a cause of the low power density and the low reliability.

The active power decoupling has been considered in order to solve problem which comes from the electrolytic capacitor [10]-[20]. The active power decoupling circuit does not require the large capacitor for the compensation of the double-line frequency power ripple. Therefore, a firm or ceramic capacitor is employed instead of the electrolytic capacitor for the decoupling capacitor. However, the additional circuit is usually required for the power decoupling operation. As the result, the conversion efficiency decreases due to losses of the additional component.

This paper proposes the active power decoupling method based on the boost converter using the Triangular Current Mode (TCM). TCM achieves the ZVS operation in order to reduce the switching losses. The proposed converter consists of the boost-converter-based active power decoupling circuit and the grid-tied inverter. The proposed TCM control is implemented in both of the converters, and it provides the power decoupling capability with the simple control. Moreover, the TCM control is applied to both of the power decoupling circuit and the grid-tied inverter. Therefore, the proposed multi-stage converter achieves the ZVS operation in all power conversion stage.

This paper is organized as follows. Firstly, the circuit configuration of the proposed converter is explained. Secondary. The control method of the proposed TCM is introduced. Finally, the simulation results are demonstrated to confirm the validity of the proposed control.

II. Circuit Configuration

Fig.1 shows the conventional DC to single-phase AC grid-tied converter with a typical DC/DC converter. The DC/DC converter has the capability of MPPT based on the current feedback control. The Voltage Source Inverter (VSI) is connected to the single-phase grid, and it provides the grid-tied operation in order to transfer the PV generated power to the single-phase grid. In the commonly configuration, the bulky electrolytic capacitor is necessary in the DC-link for the power decoupling.

Fig.2 shows the proposed circuit with DCX. The power decoupling circuit consists based on the typical boost converter. The power decoupling circuit compensates the double-line frequency power ripple by the small capacitor C_{buf}. Therefore, the bulky electrolytic capacitor in the DC-link is not necessary on the proposed circuit. DCX is placed on the input of the power decoupling circuit in order to obtain the DC voltage V_{dc} of several hundred volts.

Fig.3 shows the circuit configuration of DCX which consists of half-bridge SR converter. Each switching devices change the switching state by the duty of 50%. The switching frequency is designed to the resonance frequency of L_{res} and C_{res} in order to obtain ZVS and ZCS. As the result, the half-bridge SR converter greatly reduces the switching losses.

Fig.4 shows the relationship between the DC input power, the single-phase AC output power, and the buffer power of the decoupling capacitor. Firstly, the instantaneous AC output power p_{out} is expressed as

$$p_{out} = \frac{V_{acp} I_{acp}}{2}(1-\cos 2\omega t) \tag{1}$$

where V_{acp} is the peak AC voltage, I_{acp} is the peak AC current, ω is the grid angular frequency. According to (1), the power ripple that contains double-line frequency of the AC output power appears at DC side. Therefore, the instantaneous power of P_{buf} should be controlled by

$$p_{buf} = \frac{1}{2} V_{acp} I_{acp} \cos 2\omega t \tag{2}$$

where the polarity of p_{buf} is defined as the positive when the buffer capacitor C_{buf} discharges. Owing to the active power decoupling, the DC input power becomes constant, and it is expressed as

$$p_{in} = \frac{1}{2} V_{acp} I_{acp} = V_{in} I_{in} \tag{3}.$$

Fig.5 shows the relationship between the ripple voltage of buffer capacitor and the capacitance of C_{buf}. The buffer power in the C_{buf} is represented by

$$p_{cbuf} = \frac{1}{2}\omega C_{buf}\left\{\left(V_{ave}+\Delta\frac{V_{ripple}}{2}\right)^2-\left(V_{ave}-\Delta\frac{V_{ripple}}{2}\right)^2\right\} \tag{4}$$

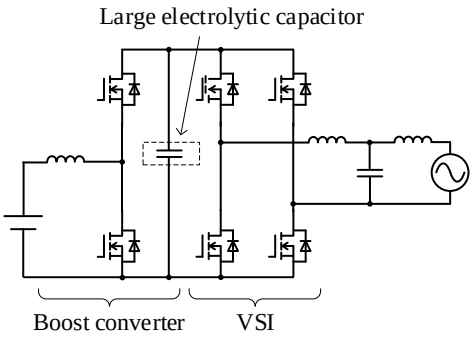

Fig.1. Circuit configuration of conventional circuit.

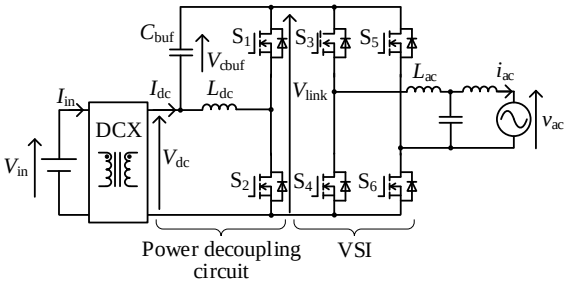

Fig.2. Circuit configuration of proposed circuit with DCX.

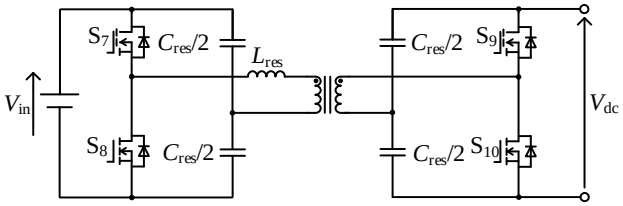

Fig.3. Circuit configuration of DCX.

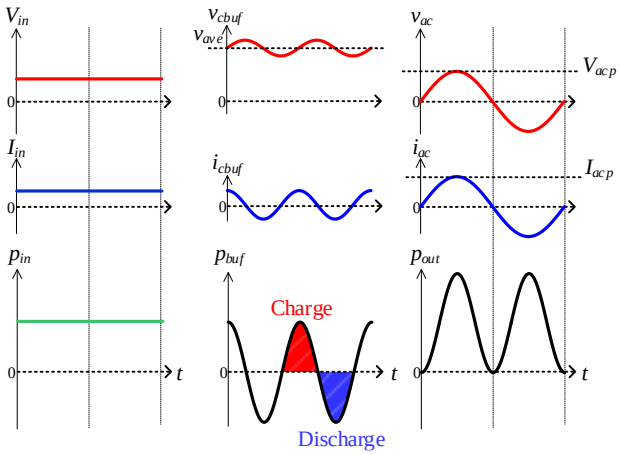

Fig.4. Relationship between DC input power, AC output power, and buffer power of energy storage.

where P_{cbuf} is the buffer power of C_{buf}, ω is the grid angular frequency, V_{ave} is the average capacitor voltage, and V_{ripple} is the ripple voltage. The capacitance for the power decoupling is calculated from (4), and it is represented by

$$C_{buf} = \frac{P_{cbuf}}{\omega V_{ave} \Delta V_{ripple}} \tag{5}.$$

According to fig.5, the capacitance for the power decoupling becomes small when the ripple voltage increases.

The active power decoupling circuit swings the buffer capacitor voltage to reduce the capacitance of C_{buf}.

III. Control Method

A. Triangular Current Mode (TCM)

Fig.6 shows the inductor current waveform in TCM and switching state of each switching devices. In the proposed circuit, TCM is implemented in both the active power decoupling circuit and VSI. The current mode of the power converter is classified into four modes of 1) Continuous Current Mode (CCM), 2) Discontinuous Current Mode (DCM), 3) Boundary Current Mode (BCM), and 4) TCM. TCM is the most simple and effective method to achieve ZVS. In TCM, the turn-on switching losses are reduced by ZVS, whereas the turn-off losses are greatly reduced by connecting a snubber capacitor in parallel with the switching devices. TCM makes the negative current period of T_{neg}. In the dead-time after T_{neg}, the parasitic capacitor of the switching devices is fully discharged owing to the negative current. As the result, ZVS is achieved when each switches is turn-on as shown in fig.6. TCM control is based on BCM control. Difference between BCM and TCM is that the negative current period is generated by the zero current detection. In BCM, the switching state is changed at the zero current. On the other hand, the switching state in TCM is delayed from the zero current in order to achieve ZVS.

B. Control method of power decoupling circuit

Fig.7 shows the control block diagram of the power decoupling circuit. TCM control is implemented based on BCM control. Both of TCM and BCM control are calculate the on-state period of $T_{on\_buf}{}^{*}$ in order to decide the average inductor current. Firstly, $T_{on\_buf}{}^{*}$ in BCM is expressed as

$$T_{on\_buf\_BCM}{}^{*} = \frac{2L_{dc}}{V_{dc\_det}} I_{ave}{}^{*} \tag{6}$$

where L_{dc} is the boost inductor, and V_{dc_det} is the detection value of DC input voltage of the power decoupling circuit, $I_{ave}{}^{*}$ is the constant current command for the I_{dc} of the DC current. Actually, $I_{ave}{}^{*}$ and I_{dc} does not match due to the parameter mismatch and the switching delay, and the power ripple. Especially, the double-line frequency power ripple fluctuates the input current of I_{dc} when the power decoupling is not applied. In particular, the dead time and the negative current in TCM are also become a cause of the error current. Therefore, the current error compensator is added in order to solve this problem. Relationship between the current command, the actual current, and the error current is expressed as

$$I_{ave}{}^{*} = I_{dc} + I_{error} \tag{7}$$

$$T_{on}{}^{*} = \frac{2L_{dc}}{V_{dc}}\left(I_{dc} + I_{error}\right) \tag{8}$$

where I_{error} is the error current between $I_{ave}{}^{*}$ and I_{dc}. Note that I_{error} becomes zero when I_{dc} is match to $I_{ave}{}^{*}$. According to (8), the compensation current of $I_{comp\_buf}{}^{*}$ is expressed as

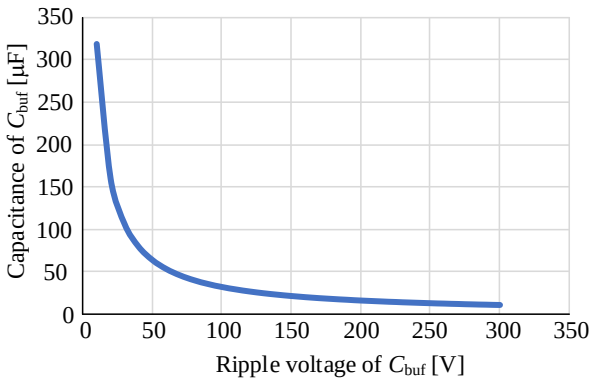

Fig.5 shows the relationship between the ripple voltage of buffer capacitor and the capacitance of C_{buf}.

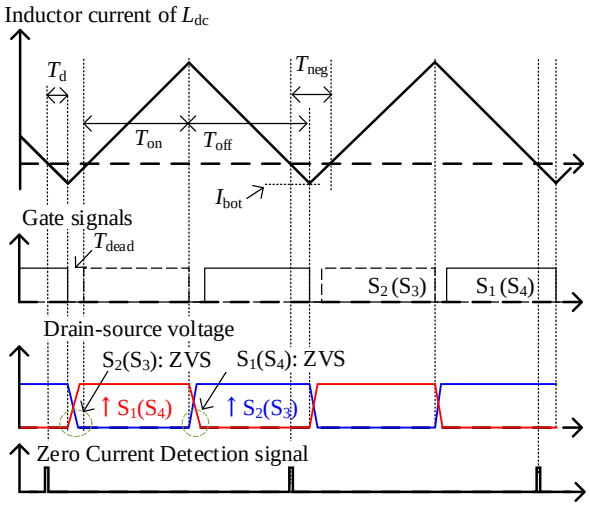

Fig.6. Inductor current waveform and switching signals in triangular current mode.

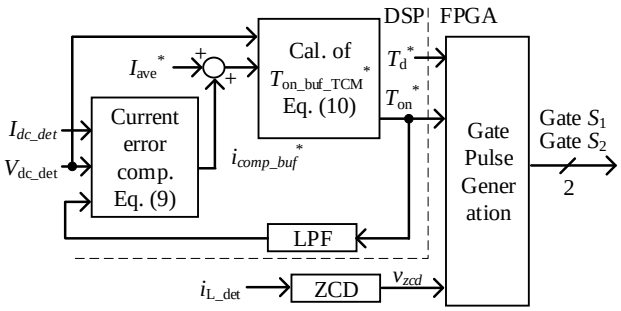

Fig.7. Control block diagram of power decoupling circuit.

$$I_{comp\_buf}{}^{*} = \frac{T_{on}{}^{*} V_{dc\_det}}{2L_{dc}} - I_{dc\_det} \tag{9}$$

where I_{dc_det} is the detection value of the DC input current of the power decoupling circuit. Finally, the on-state period in the proposed TCM is represented by

$$T_{on\_buf\_TCM}{}^{*} = \frac{2L_{dc}}{V_{dc\_det}}(I_{ave}{}^{*} + I_{comp}{}^{*}) \tag{10}$$

Owing to the current error compensator, the double-line frequency component in I_{dc} is compensated, which means that

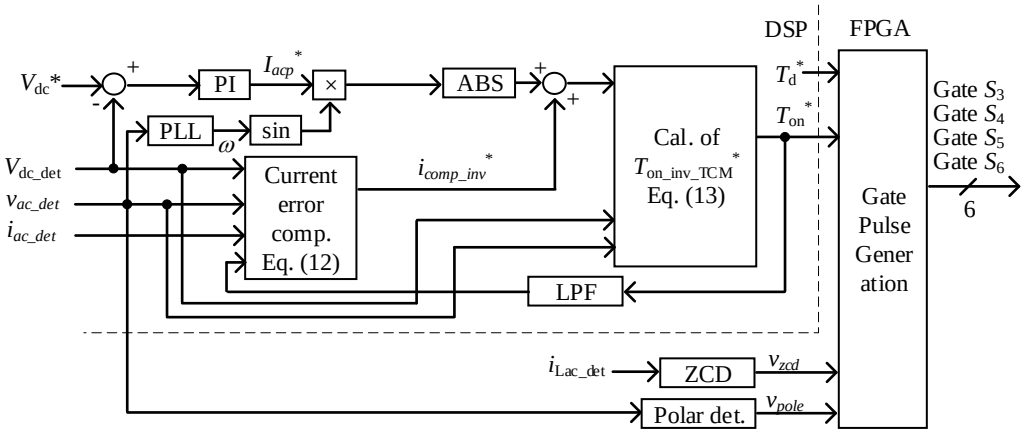

Fig.8. Control block diagram of VSI.

the active power decoupling is achieved by the proposed control. Note that T_{on}* is necessary to calculate I_{comp_buf}*. Therefore, the low-pass filter with high cut-off frequency is added on the feedback pass of T_{on}* in order to avoid the recursive calculation.

C. *Control method of grid-tied inverter*

Fig.8 shows the control block diagram of VSI. VSI is also operated with TCM to achieve ZVS. The control method of VSI is similar to the control of the power decoupling circuit. the on-state period of T_{on_inv}* in BCM and the compensation current of I_{comp_inv}* is calculated by

$$T_{on\_inv\_BCM}^{*} = \frac{2L_{ac}}{V_{dc\_det} - |v_{ac\_det}|}\left|I_{acp}^{*}\sin\omega t\right| \tag{11}$$

$$I_{comp\_inv}^{*} = \frac{T_{on\_inv}^{*}(V_{dc\_det} - |v_{ac\_det}|)}{2L_{ac}} - |i_{ac\_det}| \tag{12}$$

where I_{acp}* is the peak current command of inverter output current, L_{ac} is the inductance in the grid-tied inverter, v_{ac_det} is the detection value of the grid voltage, and i_{ac} is the detection current of the inverter output current. In VSI control, the DC-link voltage control is applied on the outer loop of TCM control. In this case, I_{acp}* is given by the output of PI controller for the voltage control. The on-state period in the proposed TCM is represented by

$$T_{on\_inv\_BCM}^{*} = \frac{2L_{ac}}{V_{dc\_det} - |v_{ac\_det}|}(\left|I_{acp}^{*}\sin\omega t\right| + I_{comp\_inv}^{*}) \tag{13}.$$

Fig.9 shows the switching state of VSI. Each gate signals for VSI is calculated by the absolute value. Therefore, the switching state of each switching devices is changed based on the grid voltage polar in order to provide the AC output current synchronized with the grid voltage as shown in fig.9.

Fig.10 shows the relationship between the bottom current I_{dc} and the switching frequency in TCM. The switching frequency of TCM decreases when the input current increases, and it is calculated by

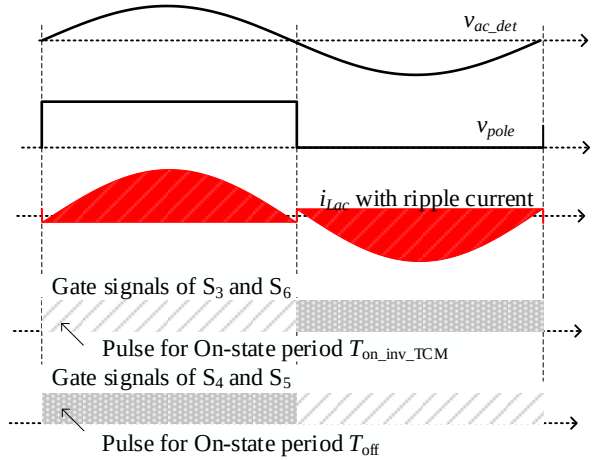

Fig.9. Switching state of VSI.

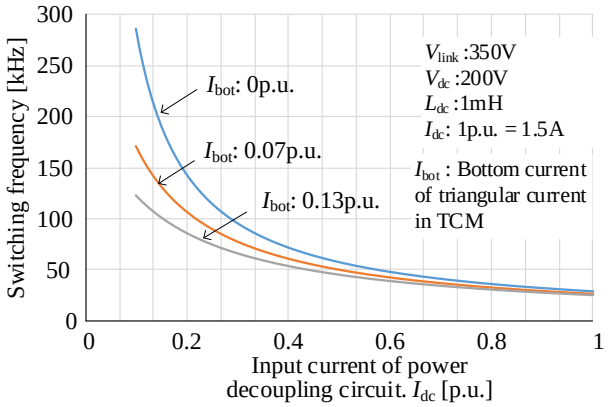

Fig.10. Relationship between bottom current I_{dc} and switching frequency.

$$f_{sw} = \frac{1}{2L_{dc}(I_{bot} + I_{ave})\left(\frac{1}{V_{link} - V_{dc}} + \frac{1}{V_{dc}}\right)} \tag{14}$$

where I_{bot} is the bottom current of the inductor current, V_{link} is the DC-link voltage. According to fig.10, the switching frequency is decreased when I_{bot} is set to large. Therefore, the bottom current in TCM influences to the ZVS characteristics and the switching frequency design.

D. Control method of DCX

DCX is operated in the open loop control of the 50% of the duty command. The switching frequency is set to the resonance frequency of L_{res} and C_{res} in fig.3. the resonance frequency is expressed as

$$f_{res} = \frac{1}{2\pi\sqrt{L_{res}C_{res}}} \tag{15}$$

where f_{res} is the resonance frequency. DCX achieves ZVS and ZCS by the series resonance of L_{res} and C_{res}.

IV. Simulation Results

Table I shows the simulation parameters, and fig.11 (a) shows the simulation result without proposed current-error-compensator. Note that the led line means that the low pass filter with 10kHz of the cutoff frequency is added to confirm the fundamental waveforms. According to fig. 11 (a), the average DC-link voltage is match to the command value of the voltage control. In addition, the sinusoidal grid current waveform is obtained by the TCM control. However, the average input current becomes low compared to the command value due to the bottom current. In particular, the input current is fluctuated at the double-line frequency due to the power ripple.

Fig.11 (b) shows the simulation result with proposed current-error-compensator. According to fig.11(b), the input current without the double-line frequency component is obtained owing to the proposed control. Especially, the average current is matched to the command value. On the other hand, the inductor current is fluctuated at the double-line frequency because the buffer capacitor is charged and discharged for the power decoupling. As the result, the ripple voltage in the DC-link voltage becomes large compared to without the proposed control. In particular, the sinusoidal grid current waveform was also obtained same as fig. 11(a). According to fig.11, the validity of the proposed control was confirmed.

Fig.12 shows the harmonic analysis result of the input current. Note that the blue line means the without proposed control, the red line means the with proposed control. According to fig.12, the input current without proposed method has 32.3% of the current error. On the other hand, this current error was completely compensated by the proposed control. As the result, the DC component with the proposed control is match to the command value. In particular, the second-order harmonics in the input current is reduced by 96.0% owing to the proposed control.

V. Conclusion

This paper proposed the active power decoupling method using closed-based TCM. TCM achieves the ZVS operation in order to reduce the switching losses. However, the input current is fluctuated at the double-line frequency due to the power ripple when the conventional open-loop based TCM is applied. The proposes the closed-loop based TCM control achieves the compensation of the double-line frequency power ripple by the current error compensation. The proposed TCM control compensates the current error between the current command and the actual current by the feedback loop. Furthermore, the second-order harmonics due to the power ripple is also compensated the proposed control. From the

Table I. Simulation parameter

Symbol	Quantity	Value
V_{in}	Input voltage	50 V
P_{in}	Input power	300 W
L_{dc}	Boost Inductor	1 mH
L_{ac}	Grid-tied Inductor	1 mH
C_{buf}	Decoupling capacitor	50 μF
V_{ac}	Grid Voltage	200 V_{rms}
Fac	Grid frequency	50 Hz
N_1:N_2	Turn ratio	1:4
I_{ave}^*	Current command	1.5A
I_{bot}	Bottom current	0.5A

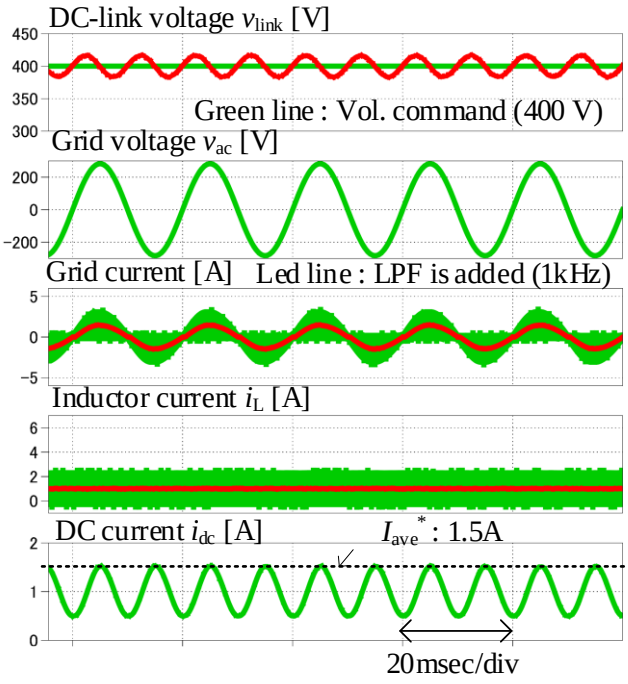

(a) Without proposed control

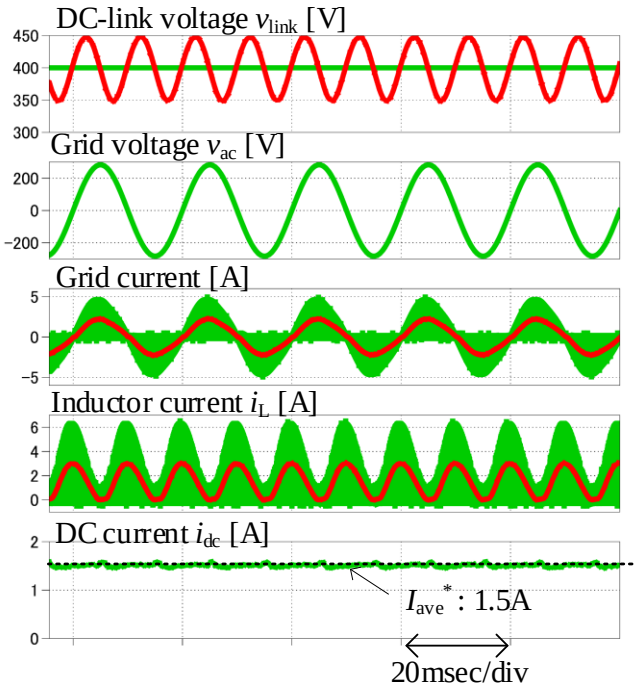

(b) With proposed control

Fig.11. Simulation results.

simulation results, it was confirmed that the current error of 32.3% was compensated by the proposed control. Finally, the second-order harmonics was reduced by 96.0%.

In the future work, the experimental result will be provided in order to confirm the validity of the proposed method.

VI. References

[1] H. Renaudineau, S. Kouro, K. Schaible and M. Zehelein: "Flyback-based Sub Module PV Microinverter", *in Proc. Eur. Conf. Power Electron*., (2016)

[2] H. Hu; Q. Zhang; X. Fang; Z. J. Shen; I. Batarseh,; "A single stage micro-inverter based on a three-port flyback with power decoupling capability" *IEEE Energy Convers. Congr. Expo.*, pp. 1411-1416, (2011)

[3] T. Shimizu, K. Wada, and N. Nakamura*;* "Flyback-type Single-Phase Interractive Inverter With Power Pulsation Decoupling on the DC Input for and AC Photovoltaic Module Systems" *IEEE Trans. Power Electron.* Vol. 21, No. 5, pp. 1264-1272, (2006)

[4] R-K. Surapaneni, A-K. Rathore: "A novel single-phase isolated PWM half-bridge microinverter for solar photovoltaic modules", *in Proc. IEEE Energy Convers. Congr. Expo.* pp. 4550-4556 (2015)

[5] E. Fonkwe, J. Kirtley, J. Elizondo: "Flyback micro-inverter with reactive power support capability", *IEEE 17th Workshop on Control and Modeling for Power Electronics*, pp.1-8 (2016)

[6] F. Ji, L. Mu, G. Zhu: "A novel Multi-function photovoltaic Micro-inverter and its control strategy", *IEEE 8th International Power Electronics and Motion Control Conference*, pp.1302-1305 (2016)

[7] Haibing Hu;Souhib Harb;Nasser Kutkut;Issa Batarseh;Z. John Shen," Power decoupling techniques for micro-inverters in PV systems-a review", *2010 IEEE Energy Conversion Congress and Exposition*, pp.3235-3240 (2010)

[8] Z. Peng;Y. Wang;X. Fei:" A Novel DC Transformer (DCX) for Single-Phase Battery Energy Storage System and Current Ripple Suppression Strategy", *2021 IEEE 12th Energy Conversion Congress & Exposition - Asia (ECCE-Asia)* (2021), pp. 1045-1050 (2021)

[9] G. Deng;Y. Sun;G. Xu;X. Chen;S. Xie;S. Yan;M. Su;Y. Liao," ZVS Analysis of Half Bridge LLC-DCX Converter Considering the Influence of Resonant Parameters and Loads", *2020 IEEE Energy Conversion Congress and Exposition*,pp.1186-1190 (2020)

[10] Yoshiya Ohnuma, Jun-ichi. Itoh: "A Single-Phase Current-Source PV Inverter With Power Decoupling Capability Using an Active Buffer",*IEEJ trans.*, Vol. 51, No. 1, pp. 531-538 (2015)

[11] X. Liu, M. Agamy, D. Dong,M. Harfman-Todorovic, L-Garces: "A low-cost solar micro-inverter with soft-switching capability utilizing circulating current", *IEEE Applied Power Electronics Conference and Exposition*, pp.3403-3408,(2016)

[12] H. Watanabe, J. Itoh: "Zero Voltage Switching Scheme for Flyback Converter to Ensure Compatibility with Active Power Decoupling Capability", *the 2018 International Power Electronics Conference*, No. 22, P1-3, pp. 896-903 (2018)

[13] C-Y Liao, W-S Lin, Y-M Chen, C-Y-Chou: "A PV Micro-inverter with PV Current Decoupling Strategy", *IEEE Trans. Power Electron.*, vol.32, No.8, pp.6544-6557, (2017)

[14] H. Han; Y. Liu; Y. Sun; M. Su; W. Xiong;"Single-phase current source converter with power decoupling capability using a series-connected active buffer" *IET Power Electron.* Vol. 8, No. 5, pp. 700-707, (2015)

[15] Y. Xia; J. Roy; R. Ayyanar;" A high performance T-type single phase double grounded transformer-less photovoltaic inverter with active power decoupling" *IEEE Energy Convers. Congr. Expo*., pp. 1-7, (2016)

[16] W. Cai; L. Jiang; B. Liu; S. Duan; C. Zou;" A Power Decoupling Method Based on Four-Switch Three-Port DCDCAC Converter in DC Microgrid" *IEEE Trans. Ind. Appl*., Vol. 51, No. 1, pp. 336-343, (2015)

[17] Ioan Serban;" Power Decoupling Method for Single-Phase H-Bridge Inverters With No Additional Power Electronics" *IEEE Trans. Ind. Electron*. Vol. 62, No.8, pp. 4805-4813, (2015)

[18] S. Qin; Y. Lei; C. Barth; W.-C. Liu; R. C. N. Pilawa-Podgurski;"A high-efficiency high energy density buffer architecture for power pulsation decoupling in grid-interfaced converters" *IEEE Energy Convers. Congr. Expo*., pp. 149-157, (2015)

[19] Y. Tang; Z. Qin; F. Blaabjerg; P. C. Loh;" A Dual Voltage Control Strategy for Single-Phase PWM Converters With Power Decoupling Function" *IEEE Trans. Power Electron.* Vol. 30, No. 12, pp. 7060-7071, (2015)

[20] Y. Tang; W. Yao; P. C. Loh; F. Blaabjerg,; "Highly Reliable Transformerless Photovoltaic Inverters With Leakage Current and Pulsating Power Elimination" *IEEE Trans. Ind. Electron*.., Vol. 63, No. 2, pp. 1016-1026, (2016)

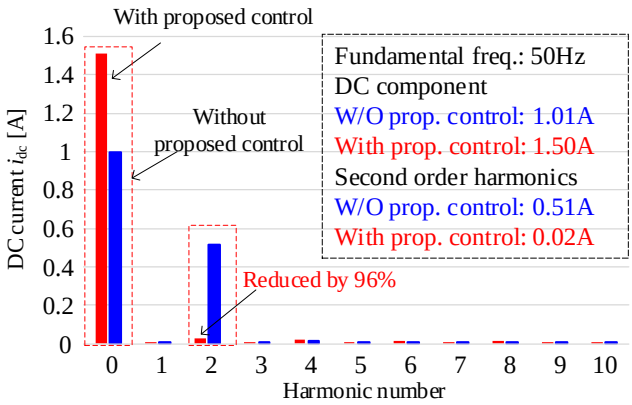

Fig.12. Harmonic analysis of input current.